Climate Dynamics (2002) 19: 555–574
DOI 10.1007/s00382-002-0249-5

T.L. Delworth · R.J. Stouffer · K.W. Dixon
M.J. Spelman · T.R. Knutson · A.J. Broccoli
P.J. Kushner · R.T. Wetherald

Review of simulations of climate variability and change with the GFDL R30 coupled climate model

Received: 5 September 2001 / Accepted: 20 March 2002 / Published online: 24 July 2002

Abstract A review is presented of the development and simulation characteristics of the most recent version of a global coupled model for climate variability and change studies at the Geophysical Fluid Dynamics Laboratory, as well as a review of the climate change experiments performed with the model. The atmospheric portion of the coupled model uses a spectral technique with rhomboidal 30 truncation, which corresponds to a transform grid with a resolution of approximately 3.75° longitude by 2.25° latitude. The ocean component has a resolution of approximately 1.875° longitude by 2.25° latitude. Relatively simple formulations of river routing, sea ice, and land surface processes are included. Two primary versions of the coupled model are described, differing in their initialization techniques and in the specification of sub-grid scale oceanic mixing of heat and salt. For each model a stable control integration of near millennial scale duration has been conducted, and the characteristics of both the time-mean and variability are described and compared to observations. A review is presented of a suite of climate change experiments conducted with these models using both idealized and realistic estimates of time-varying radiative forcing. Some experiments include estimates of forcing from past changes in volcanic aerosols and solar irradiance. The experiments performed are described, and some of the central findings are highlighted. In particular, the observed increase in global mean surface temperature is largely contained within the spread of simulated global mean temperatures from an ensemble of experiments using observationally-derived estimates of the changes in radiative forcing from increasing greenhouse gases and sulfate aerosols.

T.L. Delworth (✉) · R.J. Stouffer · K.W. Dixon · M.J. Spelman
T.R. Knutson · A.J. Broccoli · P.J. Kushner · R.T. Wetherald
GFDL/NOAA, PO Box 308,
Princeton University, Princeton, NJ 08542, USA
E-mail: td@gfdl.noaa.gov

1 Introduction

Coupled ocean–atmosphere models are among the most powerful tools to both enhance our understanding of the fundamental mechanisms of the climate system and make projections of future climate change. The development of such comprehensive models is a formidable task that should be thoroughly documented. Here we provide a review of the development and simulation characteristics of the most recent version of the global coupled climate model in use at the Geophysical Fluid Dynamics Laboratory (GFDL), as well as a brief summary of the climate variability and change experiments conducted with that model.

The philosophy of the development activity reported upon here has been to seek improvements in simulation relative to previous model versions that can be achieved through increasing spatial resolution, while maintaining the relatively simple formulation of physics from previous model versions. This design strategy leads to a model with an improved simulation of climate relative to previous model versions, but which is computationally efficient so that it can be used in a wide variety of studies of climate variability and change. Ongoing development efforts are focusing on the incorporation of new representations of physical processes.

A very important consideration has been to develop models that can run for centuries to millennia with very little climate drift. A stable multicentury control run is essential if one wishes to use such models to explore the internal variability of the coupled system on decadal and longer time scales, and is very useful in issues of climate change detection. Further, the presence of significant climate drift could alter the response of a model to changes in radiative forcing by modifying the nature of the feedbacks present in the climate system.

The outline is as follows: in Sect. 2 the model components and initialization process are described. The stability of the coupled models is described in Sect. 3 in

terms of the temporal behavior of globally and regionally averaged quantities. A comparison is made in Sect. 4 between simulated and observed characteristics of the time-mean climate, while in Sect. 5 a comparison is made between selected aspects of observed and simulated climate variability. The suite of climate change experiments conducted using these models is described in Sect. 6, along with some key results. A concluding discussion is presented in Sect. 7, along with future plans for GFDL coupled climate model development.

2 Model description

The coupled model consists of general circulation models of the atmosphere and ocean, with relatively simple formulations of land surface and sea ice processes. The model shares many formulations with previous versions of GFDL coupled climate models (see, e.g., Manabe et al. 1991), with the exception of higher spatial resolution in both the atmospheric and oceanic components. Differences in simulation characteristics between the version of the coupled model described here and previous, lower resolution versions of the model are discussed in Dixon et al. (2002).

2.1 Atmospheric component

The atmospheric component solves the primitive equations on a sphere using a spectral transform method. Fields of horizontal variables are represented by a truncated series of spherical harmonics and grid point values, with zonal truncation at wave number 30 (Rhomboidal 30 truncation, abbreviated as R30). The corresponding transform grid has a resolution of approximately 3.75° longitude by 2.25° latitude. In the vertical, a finite difference scheme is used in conjunction with a sigma (σ) coordinate system, where $\sigma = p/p^*$ is the vertical coordinate, and p^* is the surface pressure. There are 14 unevenly spaced levels extending from $\sigma = 0.9965$ near the surface to $\sigma = 0.015$ (see Table 1 for complete listing of model levels). The model uses a filtered orography (Lindberg and Broccoli 1996) to alleviate unrealistic small-scale features associated with using a finite number of spherical harmonics in the spectral representation of topography.

Precipitation is simulated whenever the predicted water content of a parcel of air exceeds saturation. The precipitation is identified to be snowfall when the air temperature near the surface is below freezing. Moist convective processes are parameterized by a moist convective adjustment scheme (Manabe et al. 1965). Over the land surface a simple "bucket" formulation is used to account for surface hydrology. At each continental grid box a budget is computed in which precipitation and snow melt are inputs of water to a "bucket" of 15 cm depth. Evaporation and sublimation remove moisture from the bucket. Evaporation is a function of both soil wetness and a potential evaporation computed assuming saturated land surface conditions (Milly 1992). Whenever the predicted water content of the bucket exceeds 15 cm total depth, the excess of water over 15 cm depth is assumed to be runoff, and is transported instantaneously to the world ocean according to a routing scheme which mimics the observed drainage basins. The water thus transported changes oceanic salinity, as discussed below.

A seasonal cycle of insolation is prescribed at the top of the atmosphere, with a solar constant of 1365 W m^{-2}. For the sake of simplicity and computational speed, no diurnal cycle of insolation is included in the model. The effects of clouds, water vapor, carbon dioxide and ozone are included in the calculation of solar and terrestrial radiation. The mixing ratio of carbon dioxide is assumed to be uniform throughout the atmosphere. Ozone is specified as a function of latitude, height, and season based on observations. Clouds are predicted whenever the relative humidity exceeds a critical threshold which varies with height (from 100% near the surface to 90% in the upper atmosphere).

Table 1. Atmospheric model levels (σ)

Level	Midpoint of layer	Thickness of layer
1	0.015	0.030 (Top)
2	0.050	0.041
3	0.100	0.060
4	0.171	0.079
5	0.257	0.094
6	0.355	0.102
7	0.460	0.108
8	0.568	0.109
9	0.675	0.105
10	0.777	0.097
11	0.866	0.082
12	0.935	0.057
13	0.979	0.029
14	0.997	0.007 (Bottom)

2.2 Ocean component

The ocean component of the coupled model uses version 1.1 of the Modular Ocean Model (Pacanowski et al. 1991). The resolution of this component is 1.875° longitude by 2.25° latitude, with 18 unevenly spaced levels in the vertical (see Table 2). The primitive equations of motion are solved numerically with the use of the Boussinesq, rigid-lid, and hydrostatic approximations.

The parameterization of processes which are not explicitly resolved on the ocean model grid plays an essential role in determining the characteristics of the model solution. For this model, horizontal and vertical mixing of momentum by subgrid scale motions are parameterized as in Bryan and Lewis (1979). Mixing of heat and salinity by subgrid scale processes occurs in two ways. The first method, after Redi (1982) and Cox (1987), is designed to mimic some of the effects of mixing of heat and salt along surfaces of constant density. In addition to this, a second "background" mixing is implemented in both the horizontal and vertical directions. As discussed later, three versions of the coupled model are described, differing in the specification of the coefficients of subgrid scale oceanic mixing and in the initialization schemes.

Whenever neighboring grid boxes in the vertical are statically unstable, their temperatures and salinities are completely mixed (Cox 1984), using six iterations per timestep. This process of

Table 2. Ocean grid box depth and thickness

Level	Depth of mid-point of grid box (m)	Thickness of grid box (m)
1	20	40 (Surface)
2	62	43
3	108	49
4	161	57
5	224	69
6	301	86
7	399	109
8	524	140
9	683	179
10	886	227
11	1142	283
12	1456	346
13	1836	413
14	2284	482
15	2798	547
16	3373	604
17	3999	648
18	4662	677 (Bottom)

convective adjustment, together with the large-scale sinking of dense water, contributes to the formation of deep water in the model oceans.

The relatively narrow waterways that connect the Mediterranean Sea and Hudson Bay to the Atlantic Ocean are not resolved by the ocean model grid. To account for these unresolved connections, a scheme is used that mixes potential temperature, salinity and any other tracers between specified non-adjacent water columns in a conservative manner (momentum is not mixed). The volume rate of mixing and the depth range are specified from observations and time invariant.

The Bering Strait is open in the model, allowing water to flow between the Pacific and Arctic oceans. However, since the Americas are not treated as an island in the computation of the barotropic stream function, the net volume of water exchanged through the Bering Strait is always zero, although non-zero advective fluxes of heat and salinity do occur between the basins.

The coupled model uses a relatively simple sea-ice model that neglects the internal pressure of the sea ice. The sea-ice model was originally developed by Bryan (1969), although modifications have been made over time, several of which are noted in Manabe et al. (1990). The horizontal grid spacing of the sea-ice model matches that of its underlying ocean model. Sea ice moves freely with the ocean currents, provided the ice thickness is less than four meters. Additional convergence of sea ice is not permitted at grid points where the thickness exceeds four meters. Sea ice changes thickness by freezing and melting of a single ice layer and by snowfall. Leads are not included in the sea ice model. The sea ice has no sensible heat content. Latent heat exchanges and freshwater fluxes associated with sea-ice formation and melting are included. Following Broccoli and Manabe (1987), the albedo of sea ice depends on surface temperature and thickness. For thick ice (at least 1 m thick), the surface albedo is 80% if the surface temperature is below –10 °C and 55% at 0 °C, with a linear interpolation between these values for intermediate temperatures. If the ice thickness is less than 1 m, the albedo decreases with a square root function of ice thickness from the thick ice values to the albedo of the underlying water surface.

The oceanic and atmospheric components interact once per day through fluxes of heat, water and momentum. The heat flux is the sum of the radiative, sensible, and latent components. The water flux consists of evaporation, sublimation, precipitation, and runoff from the continents. The runoff from a set of land points defining a river drainage basin is deposited into the ocean at the uppermost level of the ocean grid box corresponding to the "mouth" of the river. In a few cases where the river outflow is quite large (e.g., the Amazon), the "river" flow is instantaneously spread across several adjacent grid boxes in the horizontal, and the top two grid boxes in the vertical. This reduces the likelihood of numerical instabilities associated with large gradients of salinity in the ocean.

2.3 Initialization

As a first step in initializing the fully coupled model, the atmospheric component of the coupled model is integrated starting from an isothermal state at rest. Observed seasonal cycles of sea surface temperature and sea ice are used as lower boundary conditions, along with a prescribed seasonal cycle of solar radiation at the top of the atmosphere. The model is integrated for 80 years to achieve a statistical equilibrium.

As the second step, the ocean component of the coupled model is integrated for several thousand years starting from an isothermal, isohaline state at rest. The climatological seasonal cycle of the monthly mean fluxes of heat, water, and momentum archived from the atmosphere-only integration described above are supplied to the ocean as forcing terms at the sea surface. In addition, sea surface temperature (SST) and salinity (SSS), as well as sea ice, are restored to an observed climatological seasonal cycle with a restoring time of 40 days. For SST, this is the same data set used as a lower boundary condition for the atmospheric model. For the first several thousand years a numerical technique is employed to speed the convergence of this model to equilibrium (Bryan 1984). In this "accelerated" scheme, the effective heat capacities of the deep ocean layers are reduced. In addition, a much longer timestep is used for the tracer fields than for the momentum fields (a "split-time step" technique). The model is run until long term drifts in deep ocean temperature and salinity are "acceptably small", as determined subjectively.

It would be desirable for the SSTs computed by the ocean model in step 2 to match those prescribed as a lower boundary condition for the atmospheric model in step 1, since this would imply that those two component models are in approximate balance with each other (i.e., the fluxes supplied to the ocean model produce a field of SSTs which are extremely similar to those used as a lower boundary for the atmosphere). Although the model SSTs are being continuously restored toward the observed data, the SSTs computed by the ocean model generally will not match the SSTs to which they are being restored. This difference is a reflection of a fundamental imbalance between the atmospheric and oceanic components of the coupled model, and this imbalance can lead to climate drift upon coupling.

In order to reduce the likelihood of such drifts, "flux adjustment" terms are defined which are identical to the time-mean of the restoring terms in the last several hundred years of the ocean component spin up. The flux adjustments are a measure of the tendency of the ocean model to produce SSTs that are different than those experienced by the atmospheric model, and to produce SSSs that are different from observed. In the fully coupled model, these "flux adjustments" are added to the atmospheric fluxes passed to the ocean component of the coupled model. The flux adjustments attempt to compensate for the inherent mismatch between what fluxes the ocean model receives from the atmosphere, and the fluxes that the ocean model needs in order to produce a steady climate with SSTs and SSSs close to observational estimates. In this formulation, the flux adjustments are completely determined prior to the start of the coupled model integration. Thus, they do not depend on the state of the ocean during the coupled model integration, and do not systematically damp or amplify anomalies of SST or SSS. The flux adjustments vary seasonally and spatially, but are fixed from one year to the next.

Once the flux adjustments are determined, the final states of the separate ocean and atmosphere integrations are used as initial conditions for the fully coupled model (step 3). The initialization sequence described will be referred to as the "non-iterative" flux adjustment technique.

Despite the use of restoring, the SSTs computed by the ocean model during its spin up will in general differ from those used as a lower boundary condition in the atmospheric model spin up. Upon coupling, the atmospheric component of the coupled model will experience SSTs that are different from those "seen" by the atmosphere in its spin up, and this could lead to drift in the coupled system. In order to minimize this effect, an "iterative" flux adjustment initialization technique is employed. After an extended integration of the ocean model in step 2, differences remain between the model computed SSTs and the observed SSTs. A synthetic set of SSTs is derived by subtracting the simulated SSTs from the observed SSTs, and then adding that difference to the observed SSTs. The result is a set of synthetic SSTs, which differ from the observed SSTs by an amount equal in magnitude, but opposite in sign from, the model calculated SSTs. The ocean model integration is resumed, substituting the synthetic SSTs for the original observed SSTs. The desired goal is that by restoring to these synthetic SSTs, the model calculated SSTs will be closer to the observed SSTs. An analogous process is used for SSS. The ocean model integration is continued until the trends in deep ocean temperature and salinity are "acceptably" small. The revised flux adjustments and final state of the ocean model integration are then used for step 3, the fully coupled integration.

2.4 Three versions of the coupled model

Three coupled models have been constructed using the component models and initialization techniques described (see Table 3). All

Table 3. Three versions of GFDL R30 coupled model

Name	Ocean background horizontal diffusion ($cm^2\ s^{-1}$)	Ocean isopycnal diffusion coefficient ($cm^2\ s^{-1}$)	Ocean horizontal viscosity ($cm^2\ s^{-1}$)	Ocean vertical viscosity ($cm^2\ s^{-1}$)	Initialization scheme
GFDL_R30_a	1×10^6	1.9×10^7 (sfc) to 1.0×10^7 (bottom)	4×10^8	0.3 (sfc) to 1.3 (bottom)	Non-iterative
GFDL_R30_b	7.5×10^6	1.9×10^7 (sfc) to 1.0×10^7 (bottom)	1.2×10^9	0.3 (sfc) to 1.0 (bottom)	Non-Iterative
GFDL_R30_c	4×10^6	1.9×10^7 (sfc) to 1.0×10^7 (bottom)	1.2×10^9	0.3 (sfc) to 1.0 (bottom)	Iterative

have essentially the same atmospheric component, but differ slightly in the formulation of the ocean components (specification of coefficients of horizontal "background" diffusion and viscosity) and their initialization scheme. The first model will be referred to as "GFDL_R30_a" (this is the nomenclature used in the 2001 IPCC report, see Table 9.1 of Cubasch et al. 2001). This model uses the "non-iterative" initialization scheme, a horizontal background diffusion coefficient for temperature of $1 \times 10^6\ cm^2\ s^{-1}$, and a horizontal viscosity of $4 \times 10^8\ cm^2\ s^{-1}$. A control integration (constant levels of greenhouse gases) of length 120 years was performed using this model. However, after 120 years in the control integration, the model thermohaline circulation in the North Atlantic weakened substantially. This model integration was therefore not extended.

A second coupled model integration was conducted using the non-iterative initialization technique, with a background diffusivity for temperature and salinity of $7.5 \times 10^6\ cm^2\ s^{-1}$ and a horizontal viscosity of $1.2 \times 10^9\ cm^2\ s^{-1}$. This model, referred to as "GFDL_R30_b", achieved a relatively stable control integration of length 1000 years, although substantial regional drift occurred in the Atlantic basin, as discussed in the next section. In an attempt to reduce some of the regional Atlantic drift, a third coupled integration was conducted. This model, referred to as "GFDL_R30_c", used the iterative initialization technique (only one iteration was used), with a horizontal background diffusivity of $4 \times 10^6\ cm^2\ s^{-1}$ and a horizontal viscosity of $1.2 \times 10^9\ cm^2\ s^{-1}$. This model was integrated for 900 years, and produced the most stable of the three integrations in terms of ocean surface temperature drift. Since the first integration was relatively short, it will not be extensively discussed. The remainder of this study will be primarily devoted to describing the simulation characteristics of models GFDL_R30_b and GFDL_R30_c, the variety of experiments performed with those models, and reviewing some of the salient scientific studies using those experiments.

3 Stability

The stability of the two extended control integrations of the coupled models is assessed through inspection of time series of various global and regionally averaged quantities. In general, the models are quite stable and provide appropriate platforms for the study of many aspects of climate variability and change. Since climate drift is most often manifest in oceanic quantities, we emphasize these.

We note that achieving minimal drift in the coupled model solutions has been an important consideration in this model development process. The existence of a long control integration (greater than several hundred years) with minimal drift is an important pre-condition for the successful design and interpretation of climate variability and change experiments. Substantial drift over the course of an experiment can alter the base state of the model, thereby potentially altering the characteristics of the model's internal variability and its response to external forcing (Spelman and Manabe 1984). The output from long, stable control experiments provides an important database for assessing the possible range of internal variability in a model, and hence the significance of the model's response to external forcing. In the absence of sufficient observational data, such long control integrations are often used as surrogates for internal variability in the real climate system on decadal and longer time scales.

Note that a distinction is made here between models and experiments. The models (GFDL_R30_a, GFDL_R30_b, and GFDL_R30_c) refer to a specific code and a set of choices of constants for physical parameterizations (as indicated in Table 3). An experiment (as used here, and defined in Table 4) refers to the use of a specific model in combination with a specific radiative forcing type.

3.1 Global means of surface temperature, sea surface salinity, and sea ice

The time series of annual mean, global mean surface temperature (surface air temperature over continental regions, and sea surface temperature over oceanic regions) are shown in Fig. 1 from experiments CONTROL_B (extended control integration using model GFDL_R30_b) and CONTROL_C (extended control integration using model GFDL_R30_c). The long-term means were removed prior to plotting. For both experiments the drift in this quantity is relatively small, with an average drift of less than 0.2 K per 1000 years. Similarly small trends exist in the separate time series for the Northern and Southern Hemispheres. A multicentury adjustment period is also evident in each case, after which little (if any) trend exists.

The time series of global mean, annual mean, sea surface salinity (SSS) is shown in Fig. 2. Both experiments show an initial rapid drop in global mean SSS, followed by a slow recovery towards the initial conditions. The spatial pattern (not shown) of this initial change is global, with freshening in the North Atlantic, Arctic, and South Pacific. The freshening extends over the top several hundred meters of the ocean.

Time series of annual mean sea ice extent are shown in Fig. 3 for the entire globe (top), Northern Hemisphere (middle), and Southern Hemisphere (bottom). For the Northern Hemisphere there is an initial increase in CONTROL_B over the first 200 years, after which the trend is much smaller. This initial increase is related to a

Table 4. List of radiative forcing types and experiments

Experiment name	Model (described in text)	Forcing	Duration
CONTROL_A	GFDL_R30_a	Control	120 years
CO_2_1%_A	GFDL_R30_a	1%	120 years
CONTROL_B	GFDL_R30_b	Control	1000 years
2X_B	GFDL_R30_b	2X	200 years
4X_B	GFDL_R30_b	4X	300 years
GS_B_{1,2,3,4,5} [5 member ensemble]	GFDL_R30_b	GS	1865–2089 Experiments initialized from years 116,351,401,301, and 501 respectively from CONTROL_B.
GS.5_B	GFDL_R30_b	GS.5	1990–2089 Experiment initialized from year 1990 of GS_B_1
CONTROL_C	GFDL_R30_c	Control	900 years
G_C_{1,2,3} [3 member ensemble]	GFDL_R30_c	G	1865–2089 Experiments initialized from years 11,51,101 respectively from CONTROL_C
GS_C_{1,2,3} [3 member ensemble]	GFDL_R30_c	GS	1865–2089 Experiments initialized from years 11,51,101 respectively from CONTROL_C
GSS_C_{1,2,3} [3 member ensemble]	GFDL_R30_c	GSS	1865–1998 Experiments initialized from years 11,51,101 respectively from CONTROL_C
GSSV_C_{1,2,3} [3 member ensemble]	GFDL_R30_c	GSSV	1865–1998 Experiments initialized from years 11,51,101 respectively from CONTROL_C
IPCC_A2	GFDL_R30_c	IPCC_A2	1990–2100 (initialized from simulated year 1990 of GS_C_1)
IPCC_B2	GFDL_R30_c	IPCC_B2	1990–2100 (initialized from simulated year 1990 of GS_C_1)

The following entries provide descriptions of the forcing types mentioned above:
Control: The model is run with constant levels of GHGs.
1%: GHGs increase at 1% per year for the duration of the experiment.
2X: GHGs increase at 1% per year until reaching double their initial level, then are held constant.
4X: GHGs increase at 1% per year until reaching four times their initial level, then are held constant.
G: Estimates of the radiative effects of observed increases in GHGs over the period 1865–1990 are applied to the model; thereafter, GHGs are projected to increase at 1% per year.
GS: Estimates of the radiative effects of observed increases in GHGs and sulfate aerosols over the period 1865–1990 are applied to the model; thereafter, GHGs are projected to increase at 1% per year. The radiative effects of sulfate aerosols are parametrized by changes to the surface albedo. Spatial maps of altered albedo are defined for the calendar years 1986 and 2050. The altered albedo fields applied each year are determined by a linear combination of the two maps. (See Haywood et al. 1997)
GS.5: Same as *GS*, except that after 1990 GHGs are projected to increase at 0.5% per year.
GSS: Same as *GS*, except that estimates of the time-varying solar irradiance (Lean 2000) are also included.
GSSV: Same as *GSS*, except that an estimate of the radiative effects of volcanic eruptions is included. The volcanic effects are represented by latitude-dependent perturbations in incident solar radiation, based on estimates of temporal variations in the radiative forcing due to volcanic aerosols in the stratosphere (Andronova et al. 1999).
IPCC_A2: The radiative forcing changes from IPCC scenario A2 are applied over the period 1990–2100.
IPCC_B2: The radiative forcing changes from IPCC scenario B2 are applied over the period 1990–2100.

weakening of the North Atlantic thermohaline circulation during that same period, as described below, and is largely responsible for the increase in global ice extent. In contrast, drifts in sea-ice extent are much smaller in CONTROL_C (much less than 5% per 1000 years). The time-mean areal extent of Northern Hemisphere sea ice in CONTROL_C (11.7×10^6 km^2) is consistent with a range of observational estimates (Vinnikov et al. 1999) for the 20th century.

3.2 Volume mean ocean temperature and salinity

Shown in Fig. 4 are time series of volume averaged ocean temperature (Fig. 4a) and salinity (Fig. 4b) in the two extended control integrations. In both experiments temperature decreases over the course of the integration, with the decrease more pronounced in experiment CONTROL_C. A possible reason for the larger subsurface drift in CONTROL_C is that after the introduction of the "synthetic" SSTs in the initialization process for this experiment, the ocean model was not integrated as long in the spin up prior to coupling as was the case for CONTROL_B, thereby not coming as close to an equilibrium solution of the ocean model prior to coupling. The drifts in CONTROL_B and CONTROL_C correspond to long-term, global mean net heat fluxes out of the ocean of approximately 0.1 W m^{-2} and 0.2 W m^{-2}, respectively. Experiments with a multimillenial integration of a lower resolution version of this model indicate that the deep ocean takes several thousand years to fully equilibrate.

For both experiments volume mean salinity steadily decreases, implying a net addition of fresh water to the global ocean. This net fresh water addition is a result of the flux adjustments on salinity, whose global mean is non-zero. The volume mean salinity drift in CONTROL_C is somewhat smaller than that in CONTROL_B. The drifts in CONTROL_B and CONTROL_C correspond to long-term, global mean net fresh water additions to the global ocean of approximately 0.47 cm yr^{-1} and 0.24 cm yr^1, respectively.

3.3 North Atlantic thermohaline circulation

Time series of an index of the North Atlantic thermohaline circulation (THC) are shown in Fig. 5 for

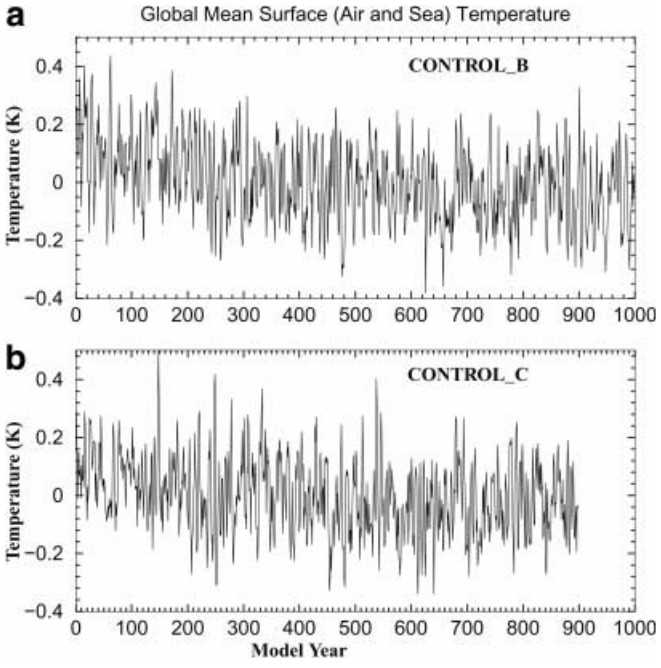

Fig. 1a, b. Time series of global mean surface temperature (surface air temperature over continental regions, and sea surface temperature over oceanic regions). The-long term means were removed prior to plotting (the mean is 288.50 for CONTROL_B and 288.45 for CONTROL_C) **a** CONTROL_B, **b** CONTROL_C

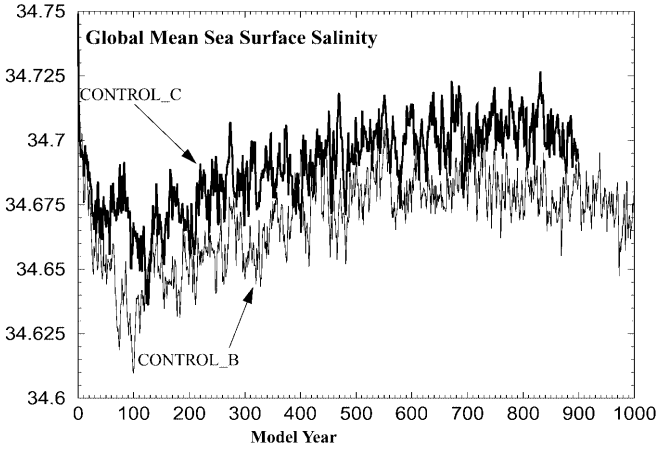

Fig. 2. Time series of global mean sea surface salinity for experiment CONTROL_B (*thin line*) and CONTROL_C (*thick line*)

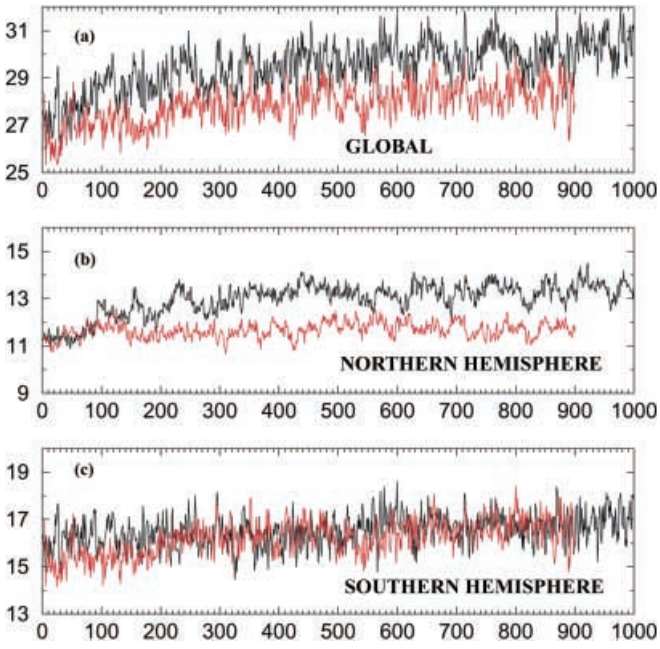

Fig. 3a–c. Time series of areal extent of sea ice (area with monthly sea ice thickness greater than 2 cm) for experiment CONTROL_B (*black line*) and CONTROL_C (*red line*). Units are 10^6 km^2. **a** Global, **b** Northern Hemisphere, **c** Southern Hemisphere

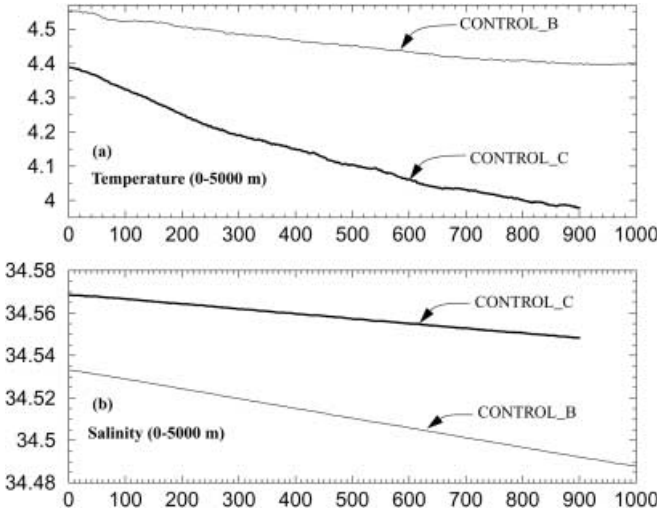

Fig. 4a, b. Time series of ocean quantities averaged over the full volume of the global ocean for experiment CONTROL_B (*heavy line*) and CONTROL_C (*thin line*). **a** Temperature, **b** salinity

experiments CONTROL_B and CONTROL_C. This index is computed each year by zonally averaging the annual mean meridional velocity across the Atlantic sector at each depth level, and then integrating these values from the ocean surface to the ocean bottom. The derivative of this stream function indicates the flow perpendicular to the direction of the derivative. The index for each year is then defined as the maximum stream function value in the Atlantic between 22°N and 90°N.

The THC index for CONTROL_B experiences a sharp drop in the latter part of the first century, falling from approximately 25 Sverdrups to 16 Sverdrups (1 Sverdrup = 10^6 m^3 s^{-1}). This drop appears to be related to a movement of fresh water anomalies from the tropical Atlantic to the subpolar regions of the North Atlantic (not shown), thereby freshening the near-surface ocean, weakening convection, and reducing the production of deep water. Analyses suggest that the development of these fresh anomalies may have been related to an imbalance between the SSTs experienced by the atmospheric model in step 1 of the initialization

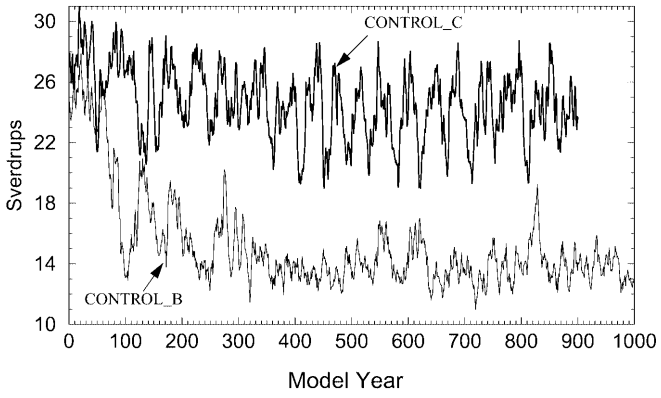

Fig. 5. Time series of thermohaline circulation index (defined in text) for the North Atlantic for experiment CONTROL_B (*heavy line*) and CONTROL_C (*thin line*). This index is computed each year by zonally averaging the annual mean meridional velocity across the Atlantic sector at each depth level, and then integrating these values from the ocean surface to the ocean bottom. The derivative of this stream function indicates the flow perpendicular to the direction of the derivative. The index for each year is then defined as the maximum stream function value in the Atlantic between 22°N and 90°N

and the SSTs calculated by the ocean model at the end of step 2 of the initialization. In addition to the initial drop, the THC time series is characterized by substantial multidecadal variability.

In contrast, the THC from experiment CONTROL_C has relatively little drift, but is characterized by substantial multidecadal variability. The nature and mechanisms of this multidecadal variability are the subject of ongoing investigations, but appear to share many features with the multidecadal North Atlantic variability seen in lower resolution versions of the GFDL climate model (Delworth et al. 1993, 1997; Delworth and Mann 2000).

3.4 Summary of stability

The suite of diagnostics presented above provide some measure of the overall stability of the coupled models. With the exception of the North Atlantic thermohaline circulation during the first 100 years in experiment CONTROL_B, the overall simulated climate system displays only very small trends. The relative stability of long control integrations is a necessary condition for the use of such models in studies of climate variability and change. In addition, such long, stable control integrations provide a rich data set for exploring simulated internal variability of the climate system, and for assessing the significance of observed and simulated climate change.

4 Simulation of time-mean climate

In this section we present an overview of the ability of the R30 GFDL coupled climate model to simulate the observed climate system. We show atmospheric quantities only from experiment CONTROL_C, since we find they are quite similar to those in CONTROL_B (with exceptions noted later). Oceanic quantities are shown from the control experiments using both models.

4.1 Sea surface temperature

Shown in Fig. 6 are differences between simulated and observed annual mean sea surface temperature (SST) for experiments CONTROL_B (Fig. 6a, average over model years 1 to 1000) and CONTROL_C (Fig. 6b, average over model years 1 to 900). For both experiments, differences are relatively small (less than 1 K in magnitude) over most of the globe. For CONTROL_B, a large region of negative SST anomalies appears in the northern North Atlantic, associated with the weakening of the THC discussed already. This bias is associated with excessive sea ice in the North Atlantic (not shown). Other notable differences occur in the subtropical eastern Pacific, where a lack of low level cloudiness leads to excessive solar radiation and positive SST anomalies. Large regional differences also occur in the circum-Antarctic.

Differences in CONTROL_C (Fig. 6b) are substantially smaller. In particular, the cold bias in the North Atlantic has been eliminated, associated with the iterative initialization technique employed. Some small regional biases remain, particularly the warm bias in the extreme southern Indian Ocean (in the region of the Kerguelen plateau), the cold bias in the central tropical Pacific where the equatorial cold tongue is too strong and extends too far across the central equatorial Pacific, and a warm bias in the eastern subtropical North and South Pacific and eastern South Atlantic.

4.2 Surface air temperature

Differences are shown between the simulated and observed continental surface air temperatures for the DJF (Fig. 7a) and JJA (Fig. 7b) seasons (the model temperatures are interpolated to a height of 2 m above the surface). During DJF the model has a cold bias over many regions of the Asian continent, particularly in a crescent stretching from northern Siberia to China and westward across the southern tier of Asia. Over North America a positive bias is seen in northwestern Canada, while a cold bias exists in the western United States. Biases in the Southern Hemisphere are relatively small.

During JJA most of the North Hemisphere continental regions exhibit a warm bias. The largest biases are in the eastern United States and central to eastern Asia. Associated with the warm bias in some areas are low values of soil moisture (not shown). Biases in the Southern Hemisphere are relatively small. The Northern Hemisphere cold bias in winter and warm bias in summer demonstrates a general tendency for the seasonal cycle of surface temperature over land to be too large in the model.

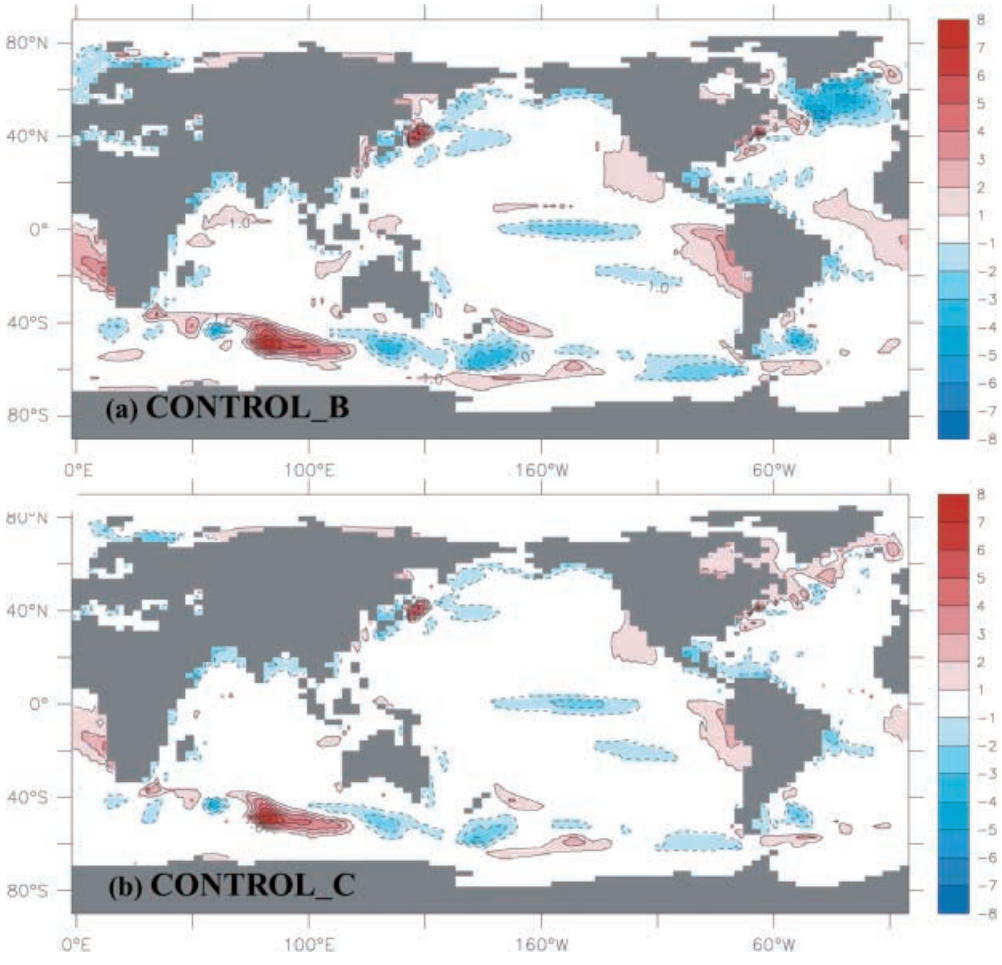

Fig. 6. **a** Differences in sea surface temperature between experiment CONTROL_B (average over years 1 to 1000) and the observations. Positive (*red*) values indicate that the simulated temperatures are warmer than those observed. Note that *white shading* denotes regions where the simulated SSTs are within 1K of the observed SSTs. **b** Same as **a** for experiment CONTROL_C (model averaged over years 1 to 900)

4.3 Precipitation

Observed (Xie and Arkin 1997) and simulated precipitation, as well as the differences between simulated and observed precipitation, are shown in Fig. 8 for both boreal winter (DJF) and summer (JJA). For both seasons the large-scale precipitation simulations capture the primary observational features, including an improved simulation of the Intertropical Convergence Zone (ITCZ) over Africa and the Atlantic during JJA relative to previous model versions with lower spatial resolution (Dixon et al. 2002). A bias common to both seasons is a tendency for excessive simulated precipitation over continental regions, with too little simulated precipitation over the oceans. Specifically during DJF, excessive precipitation is simulated over southern Africa, southeastern Asia, eastern Australia and adjacent oceanic regions, and portions of western South and Central America. In contrast, simulated precipitation is too small over many oceanic regions, with a notable exception in the western Pacific from approximately 20°S to 60°S.

During JJA there is a tendency for excessive precipitation over parts of southeast and northeast Asia, central America and northeastern North America, equatorial Africa, and portions of the tropical western Pacific. There is a broad tendency for insufficient precipitation over much of the tropical oceans, with the exception of parts of the western tropical and subtropical Pacific.

Some caution should be used in the interpretation of the above results. Simulated precipitation was also compared to the observational data set of Legates and Willmott (1990). In general, this data set has greater precipitation globally than the Xie and Arkin (1997) data set. Thus, the land precipitation bias discussed already was somewhat reduced using the Legates and Willmott (1990) observational data set as a reference, while the oceanic bias was somewhat increased. Such differences reflect uncertainty in our knowledge of the observed global precipitation distribution.

4.4 Sea level pressure

The observed and simulated distributions of sea level pressure (SLP) are shown in Fig. 9 for the DJF and JJA seasons. Note that there are substantial data limitations at higher latitudes of the Southern Hemisphere.

For both seasons the primary characteristics of the observed SLP pattern are present in the simulated SLP. During DJF the Aleutian Low is relatively more intense than observed, and centered somewhat to the east of its

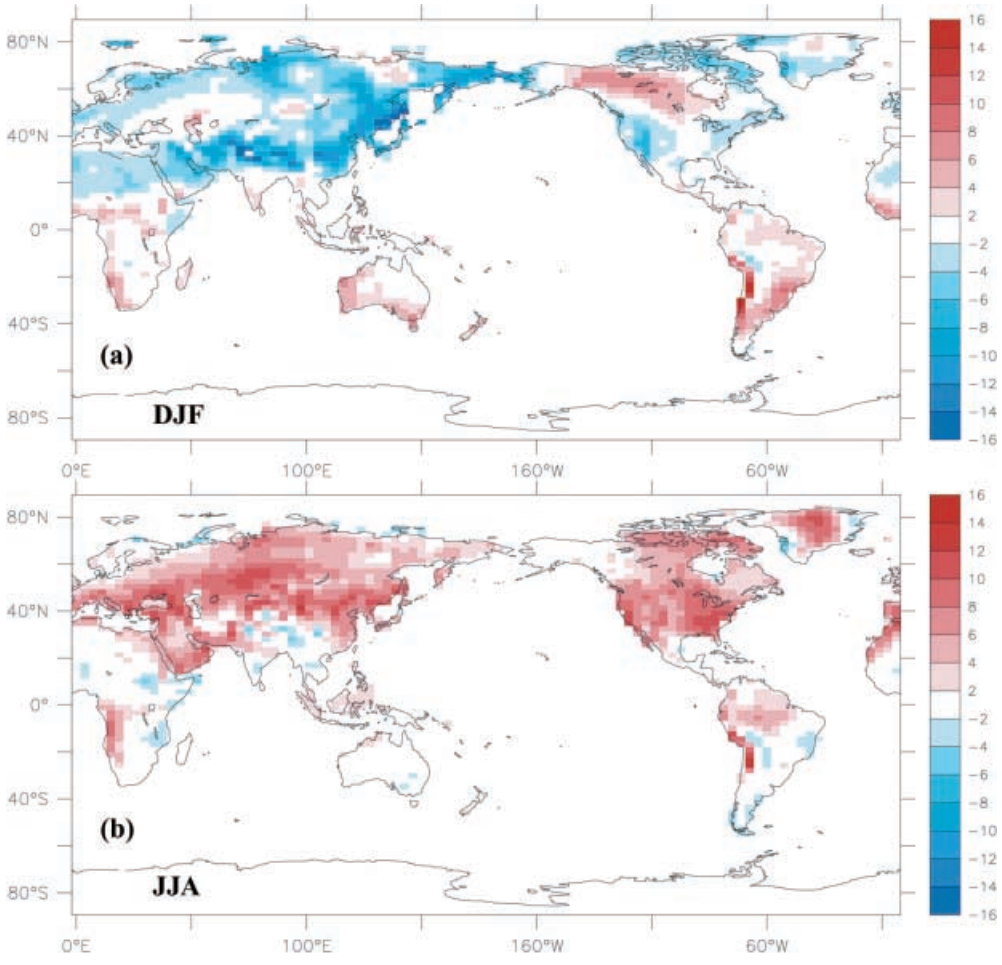

Fig. 7a, b. Differences between simulated and observed surface air temperature (positive values indicate that simulated temperatures are too high). The model results are 900 year means from experiment CONTROL_C. Units are K. **a** DJF, **b** JJA

observed positions. The simulated Icelandic Low does not extend as far into the Barents Sea region and the Arctic as observed. There is a notable deficiency in the simulation of the Beaufort High in the Arctic. The pattern and gradients of SLP in the low and middle latitudes of the Southern Hemisphere are in relatively good agreement with observations.

During JJA the Northern Hemisphere subtropical highs are in approximately the same locations as estimated from the observations, although their relative amplitudes are somewhat too large. In a similar vein, the simulated spatial pattern in the low to middle latitudes of the Southern Hemisphere is in good agreement with the observations, although the amplitudes are also somewhat too large.

5 Internal variability

5.1 Standard deviation of surface temperature

In addition to evaluating the time-mean simulated climate, we wish to document a few basic aspects of the simulated variability. Shown in Fig. 10 are maps of the standard deviation of annual mean surface temperature (see Manabe and Stouffer 1996, for a similar comparison using a lower resolution version of this coupled model). The observational analyses (Fig. 10a) use the data from Jones (1994) over land combined with the Parker et al. (1995) data set of sea surface temperatures, while in the corresponding analyses from CONTROL_C (Fig. 10b) the temperatures are from the lowest model level over land and SST over oceanic regions. Variability is clearly largest over extratropical continental regions, consistent with both the lower thermal inertia of the land surface (compared to oceanic regions) and the more vigorous extratropical atmospheric circulation in combination with large horizontal temperature gradients. In the tropical Pacific, the maximum SST variability in the simulation occurs in the middle of the basin, in contrast to the observed maximum in the eastern half of the Pacific associated with ENSO. This is one symptom of deficiencies in the simulation of tropical Pacific interannual variability (further discussion later).

Over the extratropical continents the simulated variability is generally larger than that calculated from observations, although the spatial pattern resembles the observed pattern. One notable deficiency occurs over

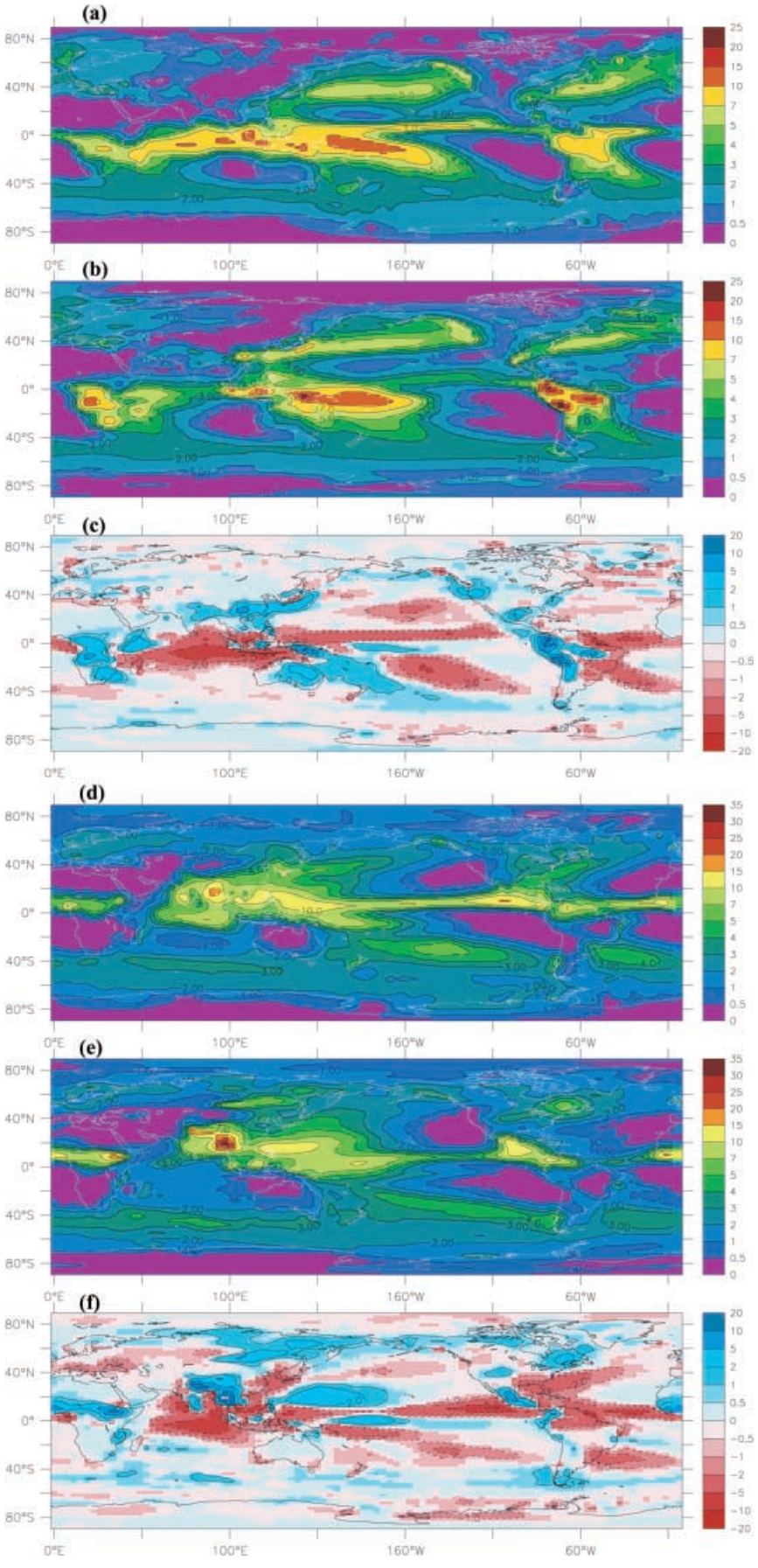

Fig. 8. **a** Observed precipitation for the months of December–February (DJF). Units are mm/day. **b** Simulated precipitation for DJF, with units of mm/day (averaged over years 1–900). **c** Simulated minus observed precipitation, units of mm/day. Positive values (*blue shading*) denotes regions where the simulated precipitation exceeds the observed precipitation. **d**–**f** Same as **a**–**c** for the months of June–August (JJA)

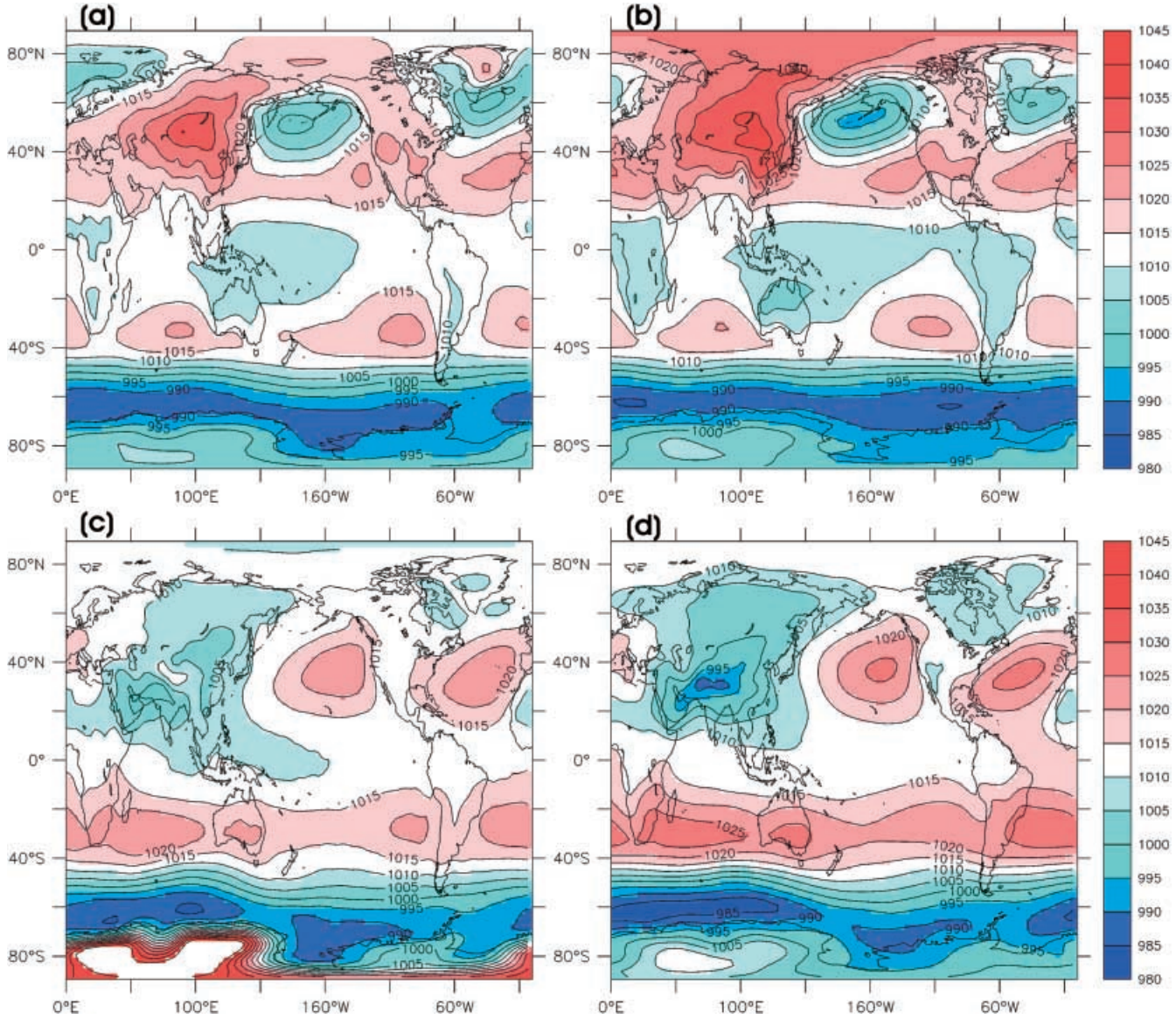

Fig. 9. **a** Observed sea level pressure (SLP) computed as a mean over the months of December–February (DJF). Units are hPa. The data is from the NCEP reanalysis over the period 1958–1997. **b** Simulated DJF sea level pressure from experiment CONTROL_C averaged over years 1 to 900. Prior to plotting in **b**, the areal means of SLP from the observations in **a** and the model are calculated over the domain 45S to 90N. The observed minus the simulated areal mean SLP is then added to the simulated SLP value at each grid point. In this manner, differences in near-global scale areal mean SLP between the observations and model are removed, and the plots highlight differences and similarities in the spatial patterns of SLP between the observations and the model. It is the gradient of SLP which is most relevant for atmospheric circulation, not the absolute values. The area south of 45S is not included in the areal mean calculations due to the sparseness of data and the orography of the Antarctic peninsula; the latter factor makes projections of pressure down to sea level somewhat arbitrary. **c** Same as **a** for the June–August season. **d** Same as **b** for the June–August season

the northwest North Atlantic, where the simulated variability in SST is substantially larger than observational estimates.

5.2 Tropical Pacific variability

As noted, the spatial pattern of the standard deviations of SST in the tropical Pacific has a maximum near the dateline, rather than in the eastern Pacific as calculated from observations. Shown in Fig. 11 are spectra of simulated and observed SST averaged over the Nino 3.4 region (170°W to 120°W, 5°S to 5°N). The observed SST is characterized by a broad peak on the 2–5 year time scale, consistent with the El-Nino Southern Oscillation phenomenon (ENSO). In contrast, the simulated peak is on the 8–9 year time scale. Additional analyses of upper ocean heat content (not shown) have revealed that this variability has a temporal evolution similar to ENSO in the sense of a delayed oscillator, despite having a time

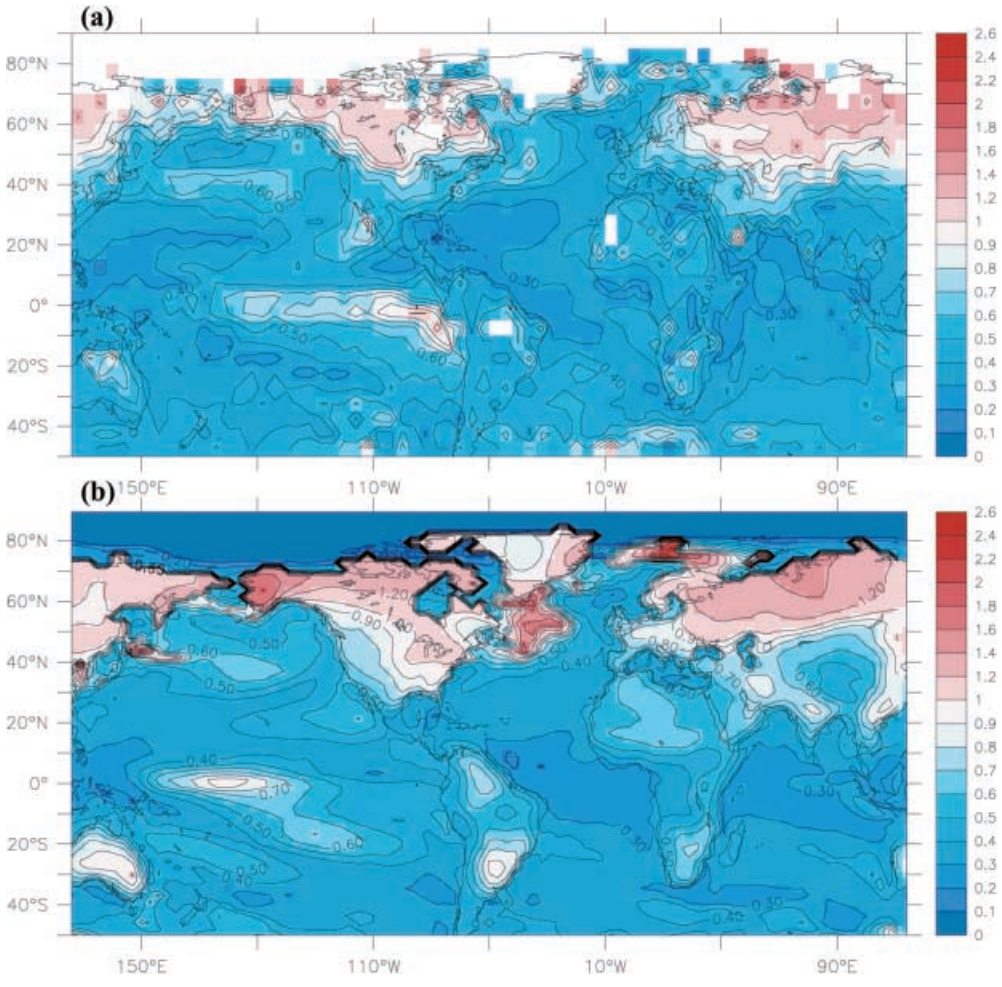

Fig. 10. **a** Standard deviation of annual mean surface temperature from observations over the period 1949–1998 (surface air temperature is used over land, and sea surface temperature is used over the ocean). For the observational data, if a grid box had fewer than four months of data in a particular year, no annual mean value was computed for that year. **b** Same as **a** for model surface temperature from experiment CONTROL_C using model years 1 to 900

scale substantially longer than that observed in the real climate system. Similar low-frequency ENSO-like behavior was investigated by Knutson and Manabe (1998) using an early version of the model (CONTROL_A). The simulated ENSO in CONTROL_C is characterized by a spatial structure with larger amplitude in the central Pacific than observed, deficient amplitude in the eastern equatorial Pacific, and a time scale that is too long. Such deficiencies may be related to the relatively coarse resolution of the model, which is insufficient for resolving some aspects of tropical Pacific ocean–atmosphere dynamics. They may also be related to the structure of the simulated time-mean tropical Pacific climate, which can influence the characteristics of the simulated interannual variability. Improving the simulation of interannual tropical Pacific variability is a high priority for future generations of GFDL coupled climate models.

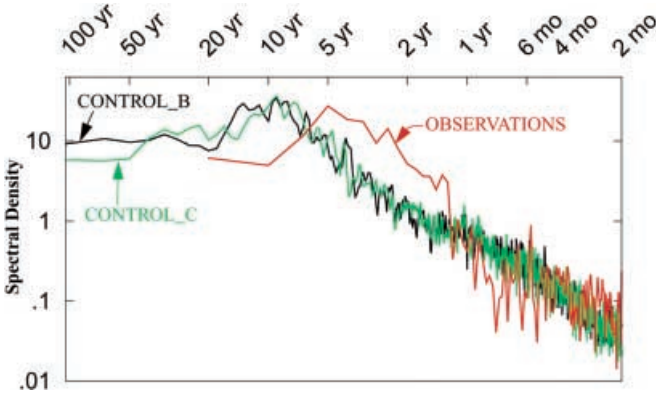

Fig. 11. Spectra of SST over the Nino 3.4 region (170°W–120°W, 5°S–5°N). The period 1949–1998 is used for the observations. *Black* (*green*) *line* is the spectrum from CONTROL_B (CONTROL_C), while the *red line* is for the observations

5.3 Arctic Oscillation

Apart from ENSO, the dominant pattern of interannual climate variability is associated with the annular modes of the extratropical atmospheric circulation field. Shown in Fig. 12 are maps of the sea level pressure (SLP) and temperature fields associated with the observed (Fig. 12a) and simulated (Fig. 12b) Arctic Oscillations (AO). The AO is defined as the first empirical orthogonal function (EOF) of sea level pressure over the domain from 20°N to 90°N. The contours indicate the sea level

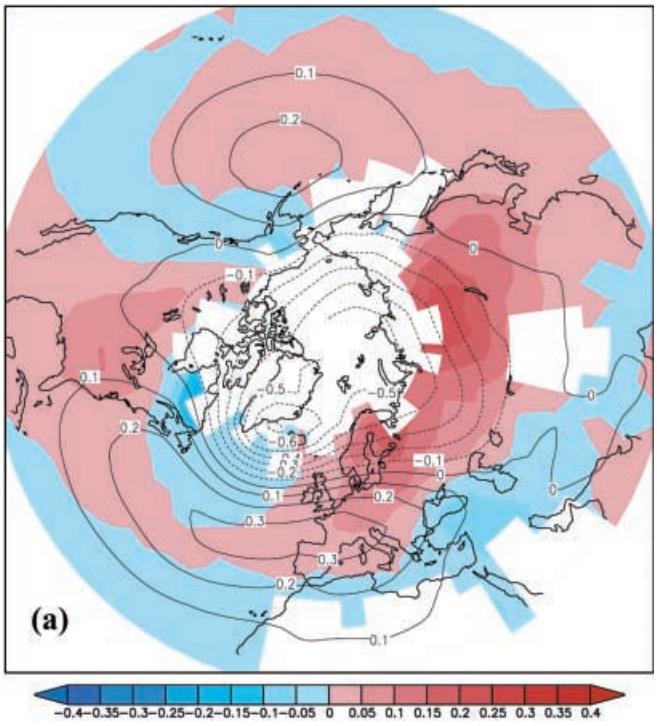

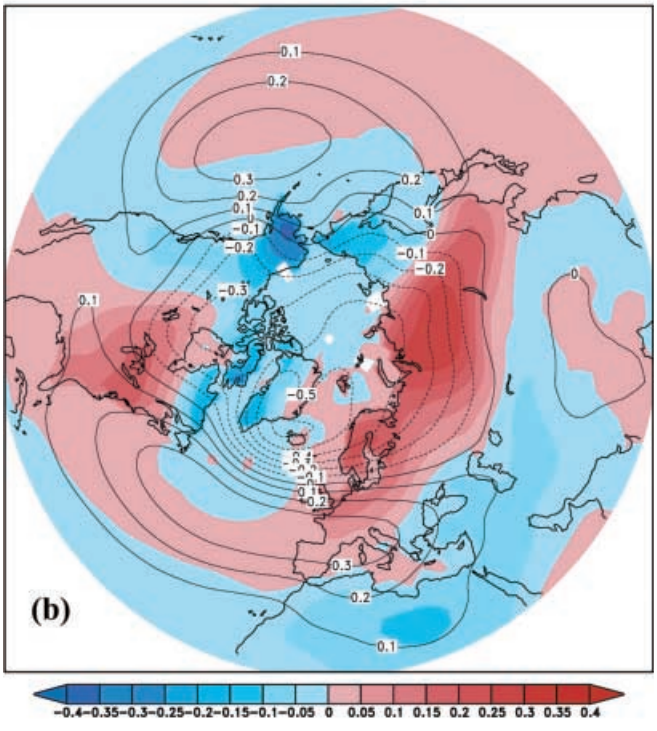

◀

Fig. 12a, b. Spatial pattern of the Arctic Oscillation (AO) and associated temperature anomalies for the months of November through April. The AO is defined by computing an empirical orthogonal function (EOF) of SLP for all points north of 20°N. An AO index is then calculated as the difference between the minimum and maximum of the spatial pattern of the first EOF multiplied by its associated time series, thereby yielding an index with units of hPa. The contours indicate the linear regression coefficients of sea level pressure (SLP) at each grid point versus an index of the AO. Units are hPa/hPa. The *color shading* indicates the linear regression coefficients of surface temperature at each grid point versus an index of the AO (surface air temperature is used over land, while SST is used over oceanic regions including ice-covered areas). Units are K/hPa. **a** Analyses from observational data (EOF of SLP adapted from Thompson and Wallace 1998; the surface temperature data is from Jones 1994). **b** Same as **a** using model output from experiment CONTROL_C for model years 1 to 900

pressure changes associated with a 1 hPa increase of an AO index, defined as the difference in sea level pressure between the Arctic and midlatitude extrema of the EOF pattern, multiplied by the EOF time series (giving an index expressed in units of hPa). The model has a highly realistic simulation of the AO, with the spatial pattern correlation between the simulated and observed pressure fields of 0.95. The color shading indicates the temperature anomalies associated with a 1 hPa increase in the AO index. Consistent with the observations, a positive phase of the simulated AO is associated with a quadrupole field of temperature anomalies, with warm anomalies over southeastern North America and northern Eurasia, and negative anomalies over northeastern North America and northern Africa through the Middle East. The primary discrepancy between the simulated and observed temperature fields related to the AO occurs over northwestern North America, with larger negative temperature anomalies in the model than observed. This is consistent with differences in the simulated and observed SLP anomaly fields over that region. The characteristics of the simulated AO and its effects on surface temperature variations have been extensively analyzed in Broccoli et al. (2001). Limpasuvan and Hartman (2000) have also compared the AO simulated by the atmospheric component of this coupled model to observational analyses, and find that the simulated AO is highly realistic.

5.4 Other aspects of simulated variability

Additional studies have examined aspects of variability simulated by the atmospheric portion of the coupled model with either prescribed SSTs or a mixed layer ocean underlying the atmosphere. These studies provide an additional evaluation of the performance of the atmospheric component of the coupled model in relation to observational analyses. Lau and Nath (1999) examined aspects of the subseasonal scale extratropical variability by examining the westward propagating, planetary scale wave observed over North America and Asia. This wave has an approximate time scale of three weeks. They report a realistic simulation of this phenomenon. Lau and Nath (2000) examined the Asian and Australian monsoon systems in this model, and found that "The essential characteristics of the model climatology for the AsianAustralian sector compare well with the observations." The model was then used to study the impact of ENSO on these monsoon systems, finding

clear linkages between ENSO variations and monsoonal rainfall and circulation. Lau and Nath (2001) and Alexander et al. (2002) have used the atmospheric portion of the coupled model to study the "atmospheric bridge" mechanism, whereby prescribed anomalies in tropical Pacific SSTs impact the extratropical atmosphere and oceans by inducing atmospheric circulation anomalies. Their analyses demonstrate that the model's extratropical atmospheric circulation responds in a realistic manner to imposed tropical SST anomalies.

6 Climate variability and change experiments

As shown in Table 4, a substantial number of climate variability and change experiments have been conducted with models GFDL_R30_b and GFDL_R30_c. In this section we wish to summarize the sets of experiments that have been completed, and some of the principal scientific findings. For a discussion comparing results from the R30 models to previous lower resolution versions of the coupled model, see Dixon et al. (2002).

6.1 Idealized forcing experiments

Two experiments were conducted using model GFDL_R30_b in order to study the response of the simulated climate system to idealized changes in radiative forcing. Atmospheric CO_2 was increased at 1% per year compounded until reaching either double (experiment 2X_B) or quadruple (experiment 4X_B) the CO_2 concentrations in the control experiment, and then held constant thereafter. Both experiments were initialized from control integration CONTROL_B (from year 116 for experiment 2X_B, and year 131 for experiment 4X_B). Experiment 2X_B is run for a total of 200 years (approximately 130 years beyond the point of CO_2 doubling), while experiment 4X_B is run for a total of 300 years (approximately 160 years beyond the point of CO_2 quadrupling).

The time series of global mean surface air temperature from both experiments is shown in Fig. 13. As documented previously (Manabe and Stouffer 1994) global temperature continues to increase after the point at which atmospheric CO_2 stabilizes (although the increase is at a much slower rate). This feature is a result of the large thermal inertia of the oceans, since the oceans take centuries to come into equilibrium with an altered radiative forcing as heat slowly penetrates the full depth of the world ocean. After 200 years the temperature increase in experiment 2X_B is approximately 3K. This is consistent with results from experiments using the same atmospheric model coupled to a slab mixed layer ocean, in which the equilibrium response to a doubling of atmospheric CO_2 is 3.4K.

Time series of an index of the North Atlantic thermohaline circulation (defined in Sect. 3.3) are shown in Fig. 14 for the two experiments. The behavior in both experiments is quite similar to that found in analogous experiments with a lower resolution (R15) version of this model (Manabe and Stouffer 1994), in which the THC weakens in response to increased precipitation and river runoff at high latitudes of the Northern Hemisphere. In experiment 4X_B the THC appears to have essentially vanished by model year 300. In the 2X_B experiment the THC has weakened substantially, but remains active even at year 200. Analogous experiments with the lower resolution version of this model suggest that the THC in the 2X_B experiment will eventually regain its original intensity, but the current experiment was not run long enough to make that determination.

An experiment in which CO_2 increases at 1% per year was also conducted using model GFDL_R30_a (experiment CO_2_1%_A in Table 4). This set of experiments was used to study tropical Pacific variability and its changes under greenhouse warming (Knutson and Manabe 1998). In addition, the simulated SSTs and atmospheric conditions from the high CO_2 climate were used as boundary conditions for a high-resolution regional hurricane model to study the impact of greenhouse warming on tropical cyclone intensities (Knutson and Tuleya 1999; Knutson et al. 2001). These studies simulated an increase in the intensity of the most severe tropical cyclones in a CO_2-warmed climate.

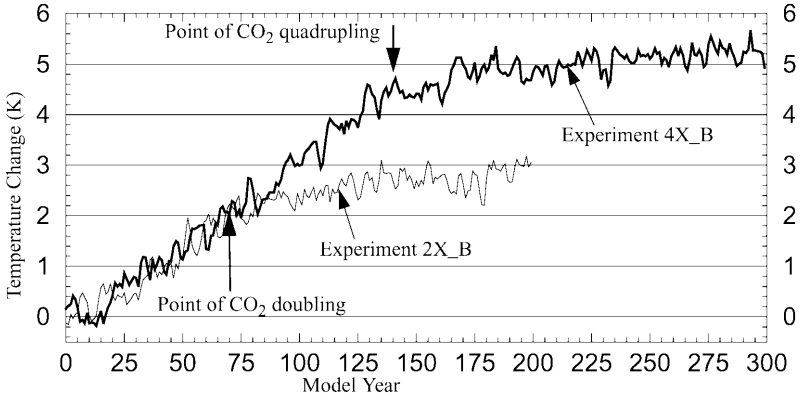

Fig. 13. Time series of annual mean, global mean surface air temperature from experiments in which CO_2 is increased at 1% per year until reaching double (quadruple) the initial concentrations, and then held constant thereafter. As per Table 4, these are the 2X_B and 4X_B experiments respectively. *Thin* (*heavy*) *line* is the 2X_B (4X_B) experiment

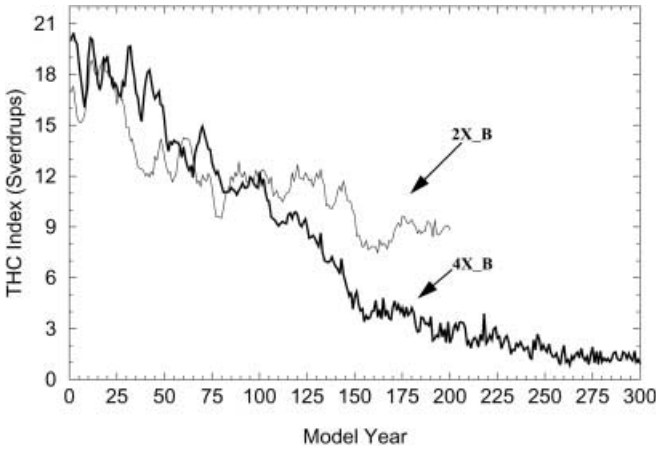

Fig. 14. Time series of the North Atlantic thermohaline circulation index (seee Fig. 5 for definition) from experiments in which CO_2 is increased at 1% per year until reaching double or quadruple the initial concentrations, and then held constant thereafter. As per Table 4, these are the 2X_B and 4X_B experiments respectively. *Thin* (*heavy*) *line* is the 2X_B (4X_B) experiment

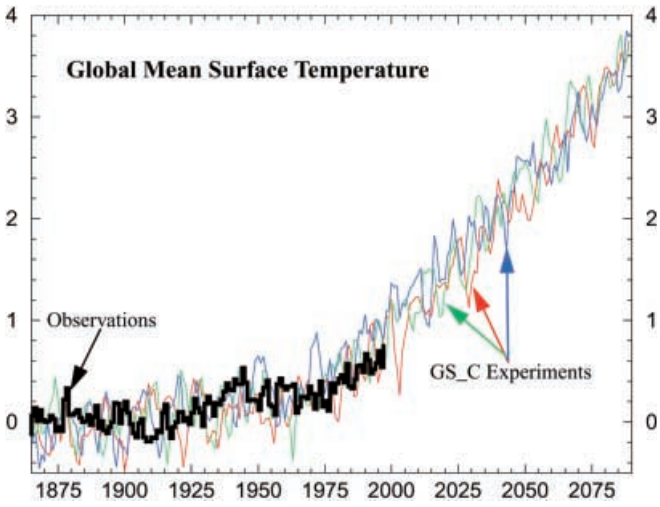

Fig. 15. Time series of annual mean, global mean surface temperature from the observations (*thick black line*) and the three member ensemble of experiments (*various colored lines*) using model GFDL_R30_c incorporating the radiative effects of increasing greenhouse gases and sulfate aerosols (experiments GS_C_{1,2,3} from Table 4)

6.2 "Realistic" forcing experiments

Ensembles of experiments have been conducted with radiative forcing designed to more closely replicate that experienced by the Earth's climate system over the late nineteenth and twentieth centuries. In these sets of experiments, an estimate of the observed time-varying concentrations of greenhouse gases (GHGs) plus sulfate aerosols is used to force the model over the period 1865–1990 (see Mitchell et al. 1995; Haywood et al. 1997). Changes in total GHGs are expressed as changes to effective CO_2, while changes in sulfate aerosols are modeled as changes to surface albedo. After 1990, effective CO_2 increases at 1% per year, while the changes to surface albedo (designed to mimic the direct effects of sulfate aerosols) vary linearly between specified maps of albedo changes for 1986 and 2050. After 2050 the albedo anomalies associated with increased sulfate aerosols are slowly reduced. This radiative forcing is based upon the IS92a scenario (Leggett et al. 1992).

An ensemble of five GHG plus sulfate aerosol experiments has been conducted using model GFDL_R30_b, and an additional set of three experiments using model GFDL_R30_c. The experiments are initialized from widely separated points in their respective control integrations. The time series of annual mean, global mean surface air temperature from the three experiments using model GFDL_R30_c are shown in Fig. 15, expressed as anomalies relative to the control integrations. Results from model GFDL_R30_b are nearly identical (shown in Delworth and Knutson 2000). The observed increase of temperature over the last century is largely within the spread of the model members, demonstrating a consistency between the simulated and observed temperature changes. The projected increase by the latter part of the twentyfirst century in global mean, annual mean temperature using this model (and the changes in radiative forcing described) is about 3K relative to present-day conditions.

The spatial pattern of surface air temperature changes is shown for DJF (Fig. 16a) and JJA (Fig. 16b). These maps are the average departures of the three ensemble members from the control integration for the period 2065–2089. Consistent with previous GFDL results (Manabe et al. 1992) and those of other groups (Cubasch et al. 2001), the warming is largest over continental regions, and at high latitudes of the winter hemisphere. During DJF and JJA relatively small warming is found in the North Atlantic, associated with a weakening of the model THC (discussed later).

During JJA the warming is largest over the continental regions, as well as the high latitudes of the Southern Hemisphere. Relatively small warming is seen at high latitudes of the Northern Hemisphere, where the partially ice-covered Arctic Ocean constrains surface air temperatures to be close to the freezing point of sea water.

The vertical distribution of atmospheric temperature change is shown in Fig. 17, where the zonally averaged changes in ensemble mean temperature are plotted as a function of latitude and height (σ) for the period 2065–2089. For DJF the amplification of the near-surface warming signal at high latitudes of the Northern Hemisphere is clear, similar to the results of Manabe and Stouffer (1994) for the annual mean. There is an additional GHG-induced maximum warming in the tropical upper troposphere, and cooling in the model stratosphere (present throughout the year).

During JJA there is little near-surface warming in the high latitudes of the Northern Hemisphere. Maximum warming again occurs in the upper troposphere of the tropics and mid to high latitudes of the Northern Hemisphere. Some evidence of near-surface polar

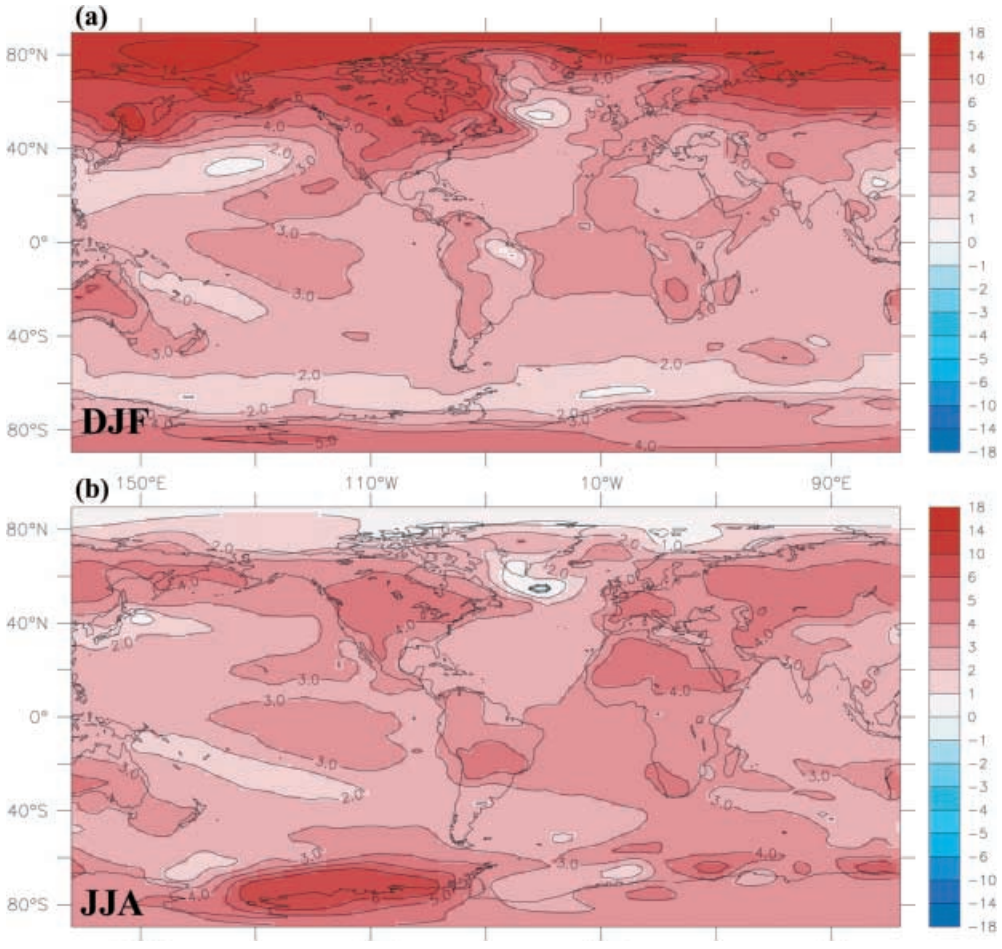

Fig. 16a, b. Spatial pattern of temperature changes for the period 2065–2089 relative to the control integration for the experiments described in Fig. 13. The map represents the ensemble mean of the GS_C_{1,2,3} experiments minus the corresponding sections of the control integrations. Positive values indicate that the GS_C ensemble mean is warmer than the control. **a** DJF **b** JJA

amplification is evident at the high latitudes of the Southern Hemisphere.

One of the primary motivations for conducting ensembles of such forced experiments is to assess the relative roles of internal variability and forced climate change for interpreting the observed climate record. Knutson et al. (1999) used the five-member ensemble from model GFDL_R30_b to assess the degree to which observed trends in regional surface temperatures were consistent with a forced climate change signal, taking into account the model's random, internal variability component. They demonstrated that for most regions of the globe the estimates of forced climate change from the GFDL coupled climate model are consistent with observed changes in surface temperature over the latter half of the twentieth century, although some significant regional differences were found. Further, the observed changes are generally inconsistent with the model's internal variability alone, strongly suggesting a role for a sustained external forcing, such as increased greenhouse gases in the late twentieth century.

In a related study, Delworth and Knutson (2000) noted that one of the five ensemble members (experiment GS_B_3) produced a simulation of global mean surface air temperature which bore a substantial resemblance to the observed temperature changes, including reproducing the rapid warming seen in the early part of the twentieth century. Their analysis concluded that such an early century rapid warming could arise from a combination of increasing greenhouse gases and an unusually large realization of internal variability of the coupled system, related in this simulation to changes in large-scale oceanic circulation in the North Atlantic. However, they also conclude that a more likely explanation of the early twentieth century warming would include a role for additional radiative forcings such as changes in solar irradiance or volcanic activity.

These sets of experiments have been extremely useful in a variety of other studies of climate change. Kushner et al. (2001) examined the response of Southern Hemisphere climate to increasing greenhouse gases, with particular emphasis on the circum-Antarctic atmospheric and oceanic circulations. The model response consisted of a summer half-year poleward shift in the westerly jet, and a year-round positive wind anomaly in the stratosphere and tropical upper troposphere. This model response projects strongly onto the model's "Southern Annular Mode" (also known as the "Antarctic Oscillation"), which is the leading pattern of variability of the extratropical zonal winds in the Southern Hemisphere. Wetherald and Manabe (2002) have used the combined set of eight experiments (GS_B

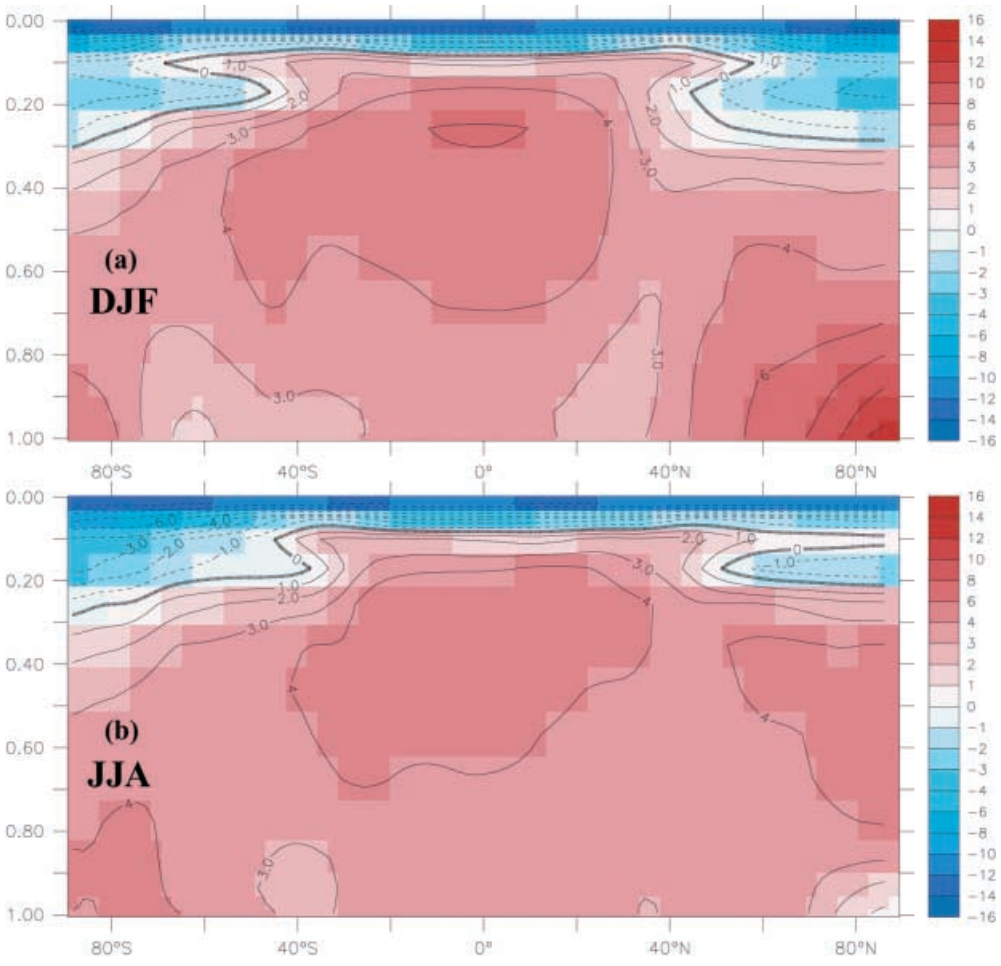

Fig. 17a, b. Differences in zonally averaged atmospheric temperature for the period 2065-2089 between the ensemble mean of the GS_C_1,2,3 experiments and the corresponding section of the control experiments

and GS_C) in studying aspects of projected hydrologic changes during the twentyfirst century, and find that many aspects of future hydrologic changes previously simulated in lower resolution versions of this coupled model are also present in the current model. Among these results is a marked increase of river outflow at high latitudes of the Northern Hemisphere. Milly et al. 2002 have used these ensembles to demonstrate a consistency between observed and simulated increases of extreme flooding in large extratropical river basins.

Two additional sets of experiments (Table 4) were performed in an effort to study the response of the climate system to solar irradiance changes and volcanic activity. The estimated changes in solar irradiance are from Lean (2000). The volcanic effects are represented by latitude-dependent perturbations in incident solar radiation, based on estimates of temporal variations in the radiative forcing due to volcanic aerosols in the stratosphere (Andronova et al. 1999). These experiments were used in Levitus et al. (2001) to compare the changes in global mean ocean heat content estimated from observations to those simulated in this model. The simulated increase in ocean heat content was similar to the observed increase when an estimate of the radiative effects of volcanic activity is included in the model, although there are substantial uncertainties in the specification of this forcing. Further, the increase in global ocean heat content estimated from the observations is inconsistent with internal variability of the coupled climate system as estimated from either CONTROL_B or CONTROL_C, lending support to the hypothesis that the observed increase in ocean heat content is at least partially attributable to human activity.

Many simulations of future climate change (Cubasch et al. 2001) indicate a reduction in the intensity of the North Atlantic thermohaline circulation in response to increasing greenhouse gases. Shown in Fig. 18 are time series of the simulated thermohaline circulation from the three GS_C experiments, as well as their ensemble mean. Consistent with experiments with a lower resolution version of this coupled model (and the results shown in Fig. 14), the North Atlantic THC weakens in response to increasing greenhouse gases, from approximately 25 Sverdrups in the late nineteenth and twentieth centuries to approximately 15–16 Sverdrups toward the latter part of the twentyfirst century. Dixon et al. (1999) have shown, using detailed analyses and additional focused experiments, that the GHG-induced weakening of the THC in a lower resolution version of the model is primarily attributable to increases in precipitation at high latitudes of the Northern Hemisphere. They also show

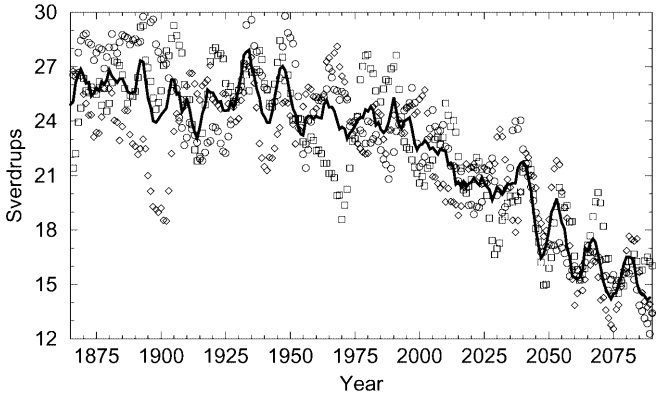

Fig. 18. Time series of an index of the North Atlantic thermohaline circulation (THC) for the ensemble of GS_C experiments. The individual experiments are denoted by the symbols (*circles*, *squares*, and *diamonds*), and the *heavy solid line* denotes their ensemble mean. Units are Sverdrups (10^6 m^3 s^{-1}). The index is defined as in Fig. 5

that some of the weakening is attributable to an additional mechanism in which the subpolar upper ocean warms (and reduces its density) through altered heat fluxes. Such detailed analyses and additional focused experiments are now being performed on the current GS runs. It is anticipated that similar processes are important, but the relative contributions of the altered heat and water fluxes need to be assessed.

Substantial decreases in Arctic sea ice are also present in the GS experiments. See Dixon et al. (2002) for a discussion of sea ice changes in these experiments.

7 Summary and discussion

Our purpose has been to provide a review of the most recently developed global coupled climate model in use at GFDL for studies of climate variability and change. The climate model consists of an atmospheric model (approximate resolution of 3.75° longitude by 2.25° latitude, 14 levels in the vertical) coupled to an ocean model (approximate resolution of 1.875° longitude by 2.25° latitude, 18 levels in the vertical), along with a relatively simple formulation of sea ice. Two primary versions were described, differing in their initialization and in the specification of the level of background horizontal mixing of temperature and salinity in the ocean component of the coupled model. In general, the atmospheric simulations of the two versions of the coupled model are nearly identical. There are differences in the oceanic simulation, with version GFDL_R30_c (see Table 3 for definition) having reduced upper ocean drift and bias. The current model provides a more realistic simulation of the mean climate in comparison to lower resolution versions of this model (see Dixon et al. 2002, for a comparison of precipitation simulations).

A review is presented of a suite of model integrations using both constant and altered levels of greenhouse gases, as well as estimates of past variations of solar irradiance and the radiative effects of changes in sulfate aerosols and volcanic activity. These integrations have been used (and are being used) for studies examining the internal variability of the climate system, and its response to altered radiative forcing. Of particular importance are studies which seek to assist in interpreting the observed climate record.

As noted in Table 4, a pair of experiments has also been conducted using the IPCC scenario forcings A2 and B2 (Cubasch et al. 2001; Mahlman and Stouffer 2002).The output from these experiments (as well as many of the other experiments described in Table 4) is publicly available on the Internet at http://nomads.gfdl.noaa.gov. Additional diagnostics of a set of experiments using the atmospheric component of the R30 coupled model are available at http://www. cdc.noaa.gov/gfdl.

Work is ongoing with these experiments to address a variety of scientific questions. Assessments are being made between observed and simulated changes in snow cover over the latter portion of the twentieth century. Detailed analyses and additional experiments are being conducted to probe the physical mechanisms associated with variability and change of the North Atlantic thermohaline circulation, including the role of freshwater forcing, as well as the influence of the North Atlantic Oscillation. Investigations are also underway on decadal to centennial hydrologic variability and change.

Extensive development work is currently underway on the next version of the GFDL coupled climate model. One of the goals of this development work is to improve upon specific physical formulations of the current model, as well as to incorporate processes not considered in the current model. This new model is expected to include new formulations of sea ice, cloud processes, land surface processes, and an improved formulation of atmospheric radiative transfer. A diurnal cycle of radiation will be included. The ocean component of the coupled model will use the latest version of the Modular Ocean Model code (MOM4) developed at GFDL. The ocean component will employ a free surface, use revised formulations of subgrid scale processes, and contain enhanced resolution in the tropical Pacific to more realistically simulate ENSO. The component models will use GFDL's "Flexible Modeling System" software framework (http://www.gfdl.noaa.gov/~fms). It is hoped that the model under development will continue our progress along a path of ever improving models of climate variability and change.

Acknowledgements The authors would like to express their collective thanks to Dr. Syukuro Manabe for his pioneering efforts in the development and use of climate models over a span of many years, and for his continuing enthusiasm and support for such work.

References

Alexander MA, Blade I, Newman M, Lanzante JR, Lau N-C, Scott JD (2002) The atmospheric bridge: the influence of ENSO

teleconnections on air–sea interaction over the global oceans. J Clim (accepted)
Andronova NG, Rozanov EV, Yang F, Schlesinger ME, Stenchikov GL (1999) Radiative forcing by volcanic aerosols from 1850 to 1994. J Geophys Res 104: 16,807–16,826
Broccoli AJ, Manabe S (1987) The influence of continental ice, atmospheric CO_2, and land albedo on the climate of the last glacial maximum. Clim Dyn 1: 87–99
Broccoli AJ, Delworth TL, Lau NC (2001) The effect of changes in observational coverage on the association between surface temperatiure and the Arctic Oscillation. J Clim 14: 2481–2485
Bryan K (1969) Climate and the ocean circulation III. The ocean model. Mon Weather Rev 97: 806–827
Bryan K (1984) Accelerating the convergence to equilibrium of ocean-climate models. J Phys Oceanogr 14: 666–673
Bryan K, Lewis LJ (1979) A water mass model of the World Ocean. J Geophys Res 84: 2503–2517
Cox MD (1984) A primitive equation, three-dimensional model of the ocean. GFDL Ocean Group Tech Rep 1, GFDL, Princeton University, Princeton, NJ, USA
Cox MD (1987) Isopycnal diffusion in a Z-coordinate ocean model. Ocean Model 74: 1–5
Cubasch U, Meehl GA, Boer GJ, Stouffer RJ, Dix M, Noda A, Senior CA, Raper S, Yap KS (2001) Projections of future climate change. In: Houghton JT, Ding Y, Griggs DJ, Noguer M, van der Linden PJ, Dai X, Maskell K, Johnson CA (eds) Climate change 2001: the scientific basis. Contribution of Working Group 1 to the Third Assessment Report of the Intergovernmental Panel on Climate Change. Cambridge University Press, Cambridge, United Kingdom, pp 881
Delworth TL, Manabe S, Stouffer RJ (1993) Interdecadal variations of the thermohaline circulation in a coupled ocean–atmosphere model. J Clim 6: 1993–2011
Delworth TL, Manabe S, Stouffer RJ (1997) Multidecadal climate variability in the Greenland Sea and surrounding regions: a coupled model simulation. Geophys Res Lett 24: 257–260
Delworth TL, Knutson TR (2000) Simulation of early 20th century global warming. Science 287: 2246–2250
Delworth TL, Mann ME (2000) Observed and simulated multidecadal variability in the Northern Hemisphere. Clim Dyn 16: 661–676
Dixon KW, Delworth TL, Spelman MJ, Stouffer RJ (1999) The influence of transient surface fluxes on North Atlantic overturning in a coupled GCM climate change experiment. Geophys Res Lett 26: 2749–2752
Dixon KW, Delworth TL, Knutson TR, Spelman ME, Stouffer RJ (2002) A comparison of climate change simulations produced by GFDL numerical models having different spatial resolutions. Global Planet Change (accepted)
Haywood JM, Stouffer RJ, Wetherald RT, Manabe S, Ramaswamy V (1997) Transient response of a coupled model to estimated changes in greenhouse gas and sulfate concentrations. Geophys Res Lett 24: 1335–1338
Jones PD (1994) Hemispheric surface air temperature variations: a reanalysis and an update to 1993. J Clim 7: 1794–1802
Knutson TR, Manabe S (1998) Model assessment of decadal variability and trends in the tropical Pacific ocean. J Clim 11: 2273–2296
Knutson TR, Tuleya RE (1999) Increased hurricane intensities with CO_2-induced global warming as simulated using the GFDL hurricane prediction system. Clim Dyn 15: 503–519
Knutson TR, Delworth TL, Dixon KW, Stouffer RJ (1999) Model assessment of regional surface temperature trends (1949–1997). J Geophys Res 104: 30,981–30,996
Knutson TR, Tuleya RE, Shen W, Ginis I (2001) Impact of CO_2-induced warming on hurricane intensities as simulated in a hurricane model with ocean coupling. J Clim 14: 2458–2468
Kushner PJ, Held IM, Delworth TL (2001) Southern hemisphere atmospheric circulation response to global warming. J Clim 14: 2238–2249
Lau N-C, Nath MJ (1999) Observed and GCM-simulated westward propagating, planetary scale fluctuations with approximately three-week periods. Mon Weather Rev 127: 2324–2345
Lau N-C, Nath MJ (2000) Impact of ENSO on the variability of the Asian–Australian monsoons as simulated in GCM experiments. J Clim 13: 4287–4309
Lau N-C, Nath MJ (2001) Impact of ENSO on SST variability in the North Pacific and North Atlantic: seasonal dependence and the role of extratropical sea-air coupling. J Clim 14: 2846–2866
Lean JL (2000) Evolution of the Sun's spectral irradiance since the Maunder minimum. Geophys Res Lett 27: 2425–2428
Legates DR, Willmott CJ (1990) Mean seasonal and spatial variability in gauge corrected, global precipitation. Int J Climatol 10: 111–127
Leggett J, Pepper WJ, Swart RJ (1992) Emissions scenarios for the IPCC: an update. In: Houghton JT, Callander BA, Varney SK (eds) Cambridge. Climate change 1992: the supplementary report to the IPCC scientific assessment. Cambridge University Press, UK, pp 69–95
Levitus S, Antonov JI, Wang J, Delworth TL, Dixon KW, Broccoli AJ (2001) Anthropogenic warming of Earth's climate system. Science 292: 267–270
Limpasuvan V, Hartmann DL (2000) Wave-maintained annular modes of climate variability. J Clim 13: 4414–4429
Lindberg C, Broccoli AJ (1996) Representation of topography in spectral climate models and its effect on simulated precipitation. J Clim 9: 2641–2659
Mahlman JD, Stouffer RJ (2002) Projection of future changes in climate. In: The Earth System: physical and chemical dimensions of global environmental change; pp 126–139. John Wiley and Sons, Chichester, United Kingdom. ISBN 0-471-97796-9
Manabe S, Stouffer RJ (1994) Multiple-century response of a coupled ocean–atmosphere model to an increase of atmospheric carbon dioxide. J Clim 7: 5–23
Manabe S, Stouffer RJ (1996) Low-frequency variability of surface air temperature in a 1000-year integration of a coupled atmosphere-ocean-land surface model. J Clim 9: 376–393
Manabe S, Smagorinsky J, Strickler RF (1965) Simulated climatology of a general circulation model with a hydrologic cycle. Mon Weather Rev 93: 769–798
Manabe S, Bryan K, Spelman MJ (1990) Transient response of a global ocean–atmosphere model to a doubling of atmospheric carbon dioxide. J Phys Oceanogr 20: 722–749
Manabe S, Stouffer RJ, Spelman MJ, Bryan K (1991) Transient response of a coupled ocean–atmosphere model to an increase of atmospheric CO_2. Part I: annual mean response. J Clim 4: 785–818
Manabe S, Spelman MJ, Stouffer RJ (1992) Transient response of a coupled ocean–atmosphere model to gradual changes of atmospheric CO_2. Part II: seasonal response. J Clim 5: 105–126
Milly PCD (1992) Potential evaporation and soil moisture in general circulation models. J Clim 5: 209–226
Milly PCD, Wetherald RT, Dunne KA, Delworth TL (2002) Increasing risk of great floods in a changing climate. Nature 415:514–517
Mitchell JFB, Johns TC, Gregory JM, Tett SFB (1995) Climate response to increasing levels of greenhouse gases and sulfate aerosols. Nature 376: 501–504
Pacanowski R, Dixon K, Rosati A (1991) The GFDL Modular Ocean Model users guide version 1, GFDL Ocean Group Tech Rep 2, pp. 44 [Available from NOAA/Geophysical Fluid Dynamics Laboratory, Princeton University, Rt. 1, Forrestal Campus, Princeton NJ 08542, USA]
Parker DE, Jones PD, Bevan A, Folland CK (1995) Interdecadal changes of surface temperature since the late 19th century. J Geophys Res 99: 14,373–14,399
Redi MH (1982) Oceanic isopycnal mixing by coordinate rotation. J Phys Oceanogr 12: 1154–1158
Spelman MJ, Manabe S (1984) Influence of oceanic heat transport upon the sensitivity of a model climate. J Geophys Res 89: 571–586

Thompson DW, Wallace JM (1998) The arctic oscillation signature in the winter time geopotential height and temperature fields. Geophys Res Lett 25: 1297–1300

Vinnikov KY, Robock A, Stouffer RJ, Walsh JE, Parkinson CL, Cavalieri DJ, Mitchell JFB, Garrett D, Zakharoz VF (1999) Global warming and Northern Hemisphere sea ice extent. Science 286: 1934–1937

Wetherald RT, Manabe S (2002) Influence of global warming upon hydrology of continents. J Geophys Res (accepted)

Xie P, Arkin PA (1997) Global precipitation: a 17-year monthly analysis based on gauge observations, satellite estimates, and numerical model output. Bull Am Meteorol Soc 78: 2539–2558